Journal of Materials Chemistry C

ROYAL SOCIETY OF CHEMISTRY

PAPER

View Article Online
View Journal | View Issue

Cite this: J. Mater. Chem. C, 2021, 9, 7643

Tuning the architectures and luminescence properties of Cu(I) compounds of phenyl and carboranyl pyrazoles: the impact of 2D *versus* 3D aromatic moieties in the ligand backbone†

Joan Soldevila-Sanmartín, [ab] Eliseo Ruiz,[c] Duane Choquesillo-Lazarte, [d] Mark E. Light,[e] Clara Viñas, [a] Francesc Teixidor, [a] Rosario Núñez, *[a] Josefina Pons [b] and José G. Planas *[a]

Incorporation of one or two *o*-carborane moieties at the backbone of the pyrazole ring was achieved by lithiation and nucleophilic addition onto the corresponding 3,5-dimethyl-1-(2-toluene-*p*-sulfonyloxyethyl)pyrazole. Two monosubstituted carboranyl pyrazoles (**L2** and **L3**) and one disubstituted carboranyl pyrazole (**L4**) were synthesized and fully characterized. All new compounds, and the corresponding monosubstituted phenylderivative (**L1**) behave as N-type ligands upon coordination with CuI to afford different polynuclear Cu(I) compounds **1–4**. Compounds **1–4** were fully characterized and their molecular structures were determined by X-ray diffraction. It is noteworthy that whereas the pyrazolylphenyl ligand **L1**, without *o*-carborane, provides a 1D coordination polymer (**1**), ligands containing carborane, **L2–L3**, affords 0D coordination compounds **2** and **3**, and disubstituted carboranyl pyrazole ligand **L4** gives rise to a 3D coordination polymer. The photoluminescence behaviour of compounds **1–4** has been investigated in the solid state and by TDDFT calculations for molecular compounds **2** and **3**. Complex **2** exhibits blue emission with a maximum at 483 nm and a high fluorescence quantum yield of 66.5%. According to TDDFT calculations the emission occurs from LUMO to HOMO−1 and HOMO−2 and deexcitation could be described as cluster-centred excited state of d–s transition in origin. This result contradicts previous studies of scarce tri-coordinated rhombohedral Cu(I) clusters, where it was assumed the origin of their emissions is (X + M)LCT in nature by analogy with tetra-coordinated rhombohedral Cu(I) clusters. Complex **3** exhibits very weak emission (Φ_F of 5%) in the green region with a maximum at 517 nm, which according to TDDFT is through a ^{3}CC state. Calculations also show that, upon excitation, **3** suffers a notable distortion resulting in the total cleavage of the Cu_4I_4 framework. This cleavage could be the cause of the relatively large Stokes shift observed for **3**. To the best of our knowledge, this is the first time that such behaviour is observed for this type of octahedral compounds. Additionally, the 1D polymer **1** exhibits weak fluorescence emission in the orange range with a maximum at 609 nm and a remarkable Stokes shift, whereas the 3D polymer **4** exhibits a similar emission to compound **2**, with a moderate quantum yield (Φ_F of 13.7%).

Received 26th March 2021,
Accepted 27th May 2021

DOI: 10.1039/d1tc01395e

rsc.li/materials-c

Introduction

Polynuclear copper(I) halide clusters have been widely investigated over decades due to their intriguing photophysical properties.[1–10] Potential applications for these materials include light-emitting devices (OLEDs),[11–13] light-emitting electrochemical cells (LECs),[14] solar cells[15] and luminescent sensors.[16,17] The interest in this family of compounds does not only stems from their photoluminescent properties, but also from the great diversity of structural motifs of the $Cu_xX_yL_z$ (X = Cl, Br, I) skeleton.[4,18] Thus, several structural motifs have been reported, ranging from 0D (coordination compounds) to 1-3D aggregates (coordination polymers).[4,12,18] For instance,

[a] *Institut de Ciència de Materials de Barcelona, ICMAB-CSIC, Campus UAB, 08193 Bellaterra, Spain. E-mail: rosario@icmab.es, jginerplanas@icmab.es*
[b] *Departament de Química, Universitat Autònoma de Barcelona, Bellaterra, 08193 Barcelona, Spain*
[c] *Departament de Química Inorgànica i Orgànica and Institut de Recerca de Química Teòrica i Computacional, Universitat de Barcelona, Diagonal 645, 08028 Barcelona, Spain*
[d] *Laboratorio de Estudios Cristalógraficos, IACT (CSIC-Universidad de Granada), Avda. de las Palmeras 4, Armilla, Granada, 18100, Spain*
[e] *School of Chemistry, University of Southampton, Highfield, Southampton SO17 1BJ, UK*

† Electronic supplementary information (ESI) available. CCDC 2048361 and 2050921–2050924. For ESI and crystallographic data in CIF or other electronic format see DOI: 10.1039/d1tc01395e

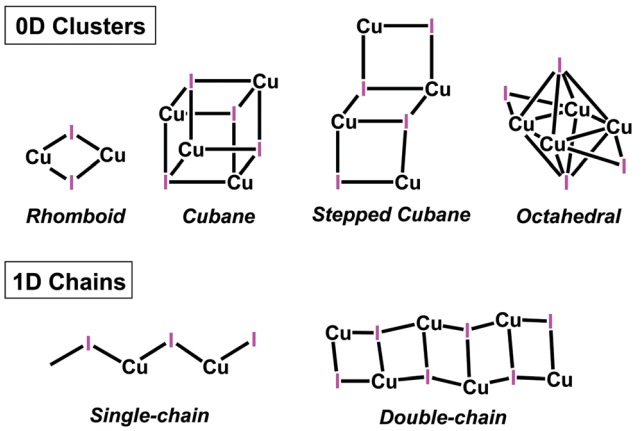

Chart 1 Schematic representation of selected CuI aggregates in copper(I) coordination compounds and polymers.

Cu_2X_2 rhomboid dimer or the Cu_4X_4 cubane and stepped-cubane are among the most common 0D structural motifs,[4,18] while octahedral Cu_4X_4 motifs are less common[19] (Chart 1). Regarding higher dimension aggregates, typical structural motifs include single-, double-, looped-, helical-chains, ribbons, columns, *etc.*[16,18,20]

These different nuclear multiplicities and aggregate dimensionalities are not only intriguing *per se*, but are also interesting because their structural parameters greatly affect the photophysical properties of the resulting compounds. For instance, in cubane-like clusters a dual emission is observed arising from two different excited states. An halide-to-ligand charge transfer (^{3}XLCT, sometimes mixed with metal-to-ligand charge transfer, ^{3}MLCT) gives rise to a high energy (HE) emission (*ca.* 450 nm) while Cu_4I_4 cluster-centred (^{3}CC) excited state yields a low energy (LE) emission (*ca.* 600 nm), which is related to the Cu–Cu distances.[4,21] In fact, this relationship between Cu–Cu distance and the LE emission gives raise to one of the most interesting properties of cubane compounds: thermochromism.[22] However, this LE emission can be quenched using rigid ligands that prevent cluster relaxation, thus "blocking" this emission,[23] or fine-tuned using different heterocyclic donors.[24] In contrast, stair-step clusters only show HE emission, due to having longer Cu–Cu distances.[25] Regarding octahedral compounds, reports including photophysical studies are much scarcer, with fewer than a dozen papers published on the subject.[19,23,25–31] This can be attributed to the fact that octahedral cores are energetically unfavourable compared to the cubane cores, as demonstrated by theoretical calculations.[28] Optical properties of these octahedral compounds have also been studied and various reports suggest that the rigidity and steric demands of the ligands seems to play a more significant role in the photophysical properties than in the cubane type clusters.[19]

With regards to the ligands employed in the above mentioned polynuclear Cu(I) halides, nitrogen- (N-), sulfur- (S-) and phosphorus- (P-ligands) containing ligands are commonly found.[4,5,18,32] Structures with N-ligands (either monodentate or multidentate) are by far more common and show intriguing luminescent properties.[25,33] Reported examples on octahedral motifs include bidentate ligands bearing small angles (*e.g.*, P^N,[23,25,27,28,30] P^P,[26,29,31,34–37] C^P[38] and N^N[19]), with only one example based on a monodentate N-heterocyclic carbene ligand.[39] Within the family of polynuclear Cu(I) compounds containing N-ligands, pyrazoles are significantly less studied than the overwhelming family of pyridines.[32] Furthermore, pyrazole ligands employed in such polynuclear Cu(I) compounds are deprotonated (pyrazolate ligands) or neutral pyrazolyl-pyridine/pyrimidine combinations.[32,40–44] To our knowledge, there is only one report on a neutral monodentate only-pyrazole (not having other nitrogenated substituents) based Cu(I) complex.[45] There are however some more reports on neutral poly-pyrazolyl ligands, leading to a wide variety of coordination polymers.[46–49]

As part of our on-going research on pyrazole[50–55] and carborane[56–63] based ligands for functional metal compounds, we were interested in exploring the impact of adding the icosahedral carborane clusters to the pyrazole fragment on the coordination to Cu(I) ions and the corresponding luminescence properties. Icosahedral carboranes 1,*n*-$C_2B_{10}H_{12}$ (n = 2, 7 or 12) are a class of commercially available and exceptionally stable 3D-aromatic boron-rich clusters that possess material-favourable properties such as thermal and chemical stability and high hydrophobicity.[64–66] Neutral carboranes are remarkably robust boron clusters with two carbon atoms and possess 26 electrons for 12 vertices. The delocalized electron density is not uniform through the cage, giving rise to extraordinary differences in the electronic effects of the cluster.[67] This unusual electronic structure is often highlighted by regarding carboranes as inorganic three-dimensional "aromatic" analogues of arenes.[68,69] The average size of the *o*-carborane (148 Å^3) is comparable to that of adamantane (136 Å^3) and is significantly larger (40%) than the phenyl ring rotation envelope (102 Å^3).[70] Regarding the electronic effect, *o*-carborane behaves as a strong electron-withdrawing group (similar to fluorinated aryl) on a substituent at one of the cluster carbons.[70–74] Thus, introduction of the carborane moiety into a ligand backbone is expected to exert a weaker metal–heteroatom interaction with respect to the related phenyl derivative.[58,74,75] In addition, and different from classical rigid flat aromatic ligands, spherical-based linkers have access to extensive conformational space by a combination of low-energy torsion of the substituents (*e.g.*, aliphatic) and by the spherical core of the linker.[76] Thus, for example, a spherical ligand shape such as carborane could prevent the formation of intermolecular π–π staking interactions while favouring the weak dihydrogen bond interactions.[77,78] Furthermore, a remarkable influence of the carboranes on the photophysical properties of luminescence materials has also been demonstrated.[79,80] When *o*-carborane is linked to an aryl donor group, an intramolecular charge transfer (ICT) process occurs from the donor moiety to the acceptor cluster, which is influenced by the $C_{cluster}$–$C_{cluster}$ (C_c–C_c) bond vibration,[81] usually producing a quenching of the fluorescence in solution. Moreover, these systems exhibit aggregation-induced emission (AIE) in aggregate and solid states, due to a restriction of the molecular motion, which produces an important increase of the emission quantum

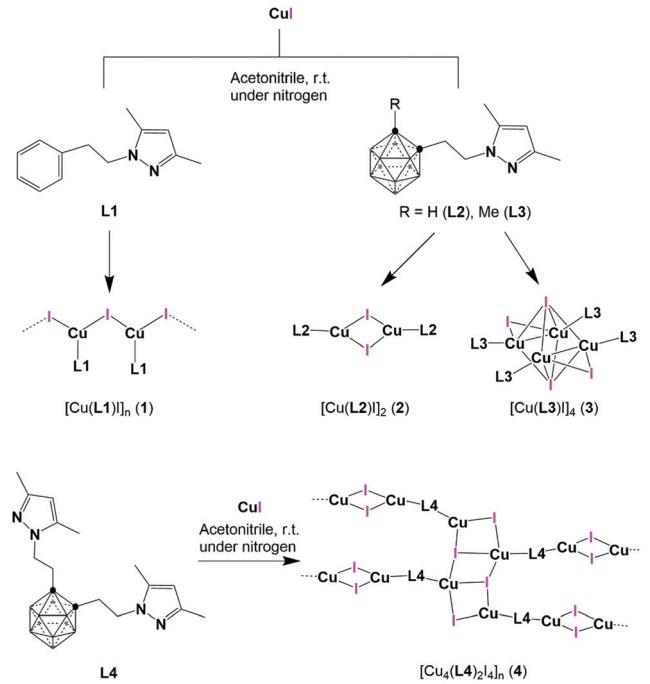

Scheme 1 Representation of pyrazole ligands **L1–L4** and their Cu(I) compounds **1–4**.

yield.[82–85] It is also noteworthy that the design of carborane–C_c-containing fluorophores whose fluorescence quantum yield in solution can be tailored by the cluster isomer (*ortho*- or *meta*-carborane) and the substituent at the C_c atom. Some of these systems show moderate to good fluorescence emission efficiency in solution and solid state, giving rise to fluorescent materials in both states.[86–91]

Herein we report the synthesis of three new pyrazolyl-carborane derivatives and their Cu(I) compounds. We also report a new Cu(I) derivative of a commercially available *N*-substituted phenyl pyrazole ligand (**L1**) that was taken for comparison between 2D and 3D aromatic groups (Scheme 1). We present the synthesis, structural characterization, and photophysical properties in solid state for all compounds. Additionally, photophysical properties for the molecular coordination compounds have been analysed by TDDFT calculations.

Results and discussion

Synthesis and characterization

Three new *N*-substituted carboranyl pyrazole ligands, derived from *o*-carborane, **L2–L4** (Scheme 1), were prepared by the reaction of lithiated *o*-carborane with the corresponding 3,5-dimethyl-1-(2-toluene-*p*-sulfonyloxyethyl)pyrazole at low temperature (see ESI† for details). All carboranyl pyrazole ligands were fully characterized by standard spectroscopic and analytical techniques (ESI,† Fig. S1–S16) and the structure of **L3** has been solved by single crystal X-ray diffraction (SCXRD; Fig. S17, ESI†). Reactions of the phenyl pyrazole ligand **L1** or the carboranyl pyrazole ligands (**L2–L4**) with anhydrous CuI in dry acetonitrile under nitrogen provided crystalline compounds **1–4** in good yields (Scheme 1). FTIR-ATR spectra showed the characteristic signals in the region from 1556 to 650 cm^{-1} that belong to vibrations of the pyrazole ring (Pz) and of the *N*-substituted pyrazole derivatives.[92,93] Carborane based compounds **2–4** show the characteristic broad B–H stretching bands from the carborane (in the range 2572–2563 cm^{-1}; Fig. S18–S21, ESI†). Crystal structures of these Cu(I) compounds were determined by SCXRD (*vide infra*), and their simulated

Table 1 Crystal and structure refinement data for **L3** and compounds **1–4**

Compound	**L3**	**1**	**2**	**3**	**4**
Empirical formula	$C_{10}H_{24}B_{10}N_2$	$C_{13}H_{16}CuIN_2$	$C_{18}H_{44}B_{20}Cu_2I_2N_4$	$C_{20}H_{48}B_{20}Cu_2I_2N_4$	$C_{34}H_{67}B_{20}Cu_4I_4N_9$
Formula weight	280.41	390.72	913.65	941.70	1579.92
Crystal system	Monoclinic	Monoclinic	Triclinic	Triclinic	Monoclinic
Space group	$P2_1/c$	$P2_1/c$	$P\bar{1}$	$P\bar{1}$	$P2_1/c$
CCDC	2048361	2050921	2050922	2050923	2050924
Unit cell dimensions					
a (Å)	10.8644(2)	4.2749(3)	10.361(2)	12.0222(8)	13.3779(13)
b (Å)	20.6842(3)	19.9244(15)	12.195(2)	12.9633(8)	19.272(2)
c (Å)	7.79360(10)	16.0826(11)	15.412(3)	14.3391(9)	23.825(2)
α (°)			98.412(6)	72.561(2)	90.0
β (°)	106.795(2)	97.106(2)	91.117(6)	78.697(2)	9.679(2)
γ (°)			96.772(6)	64.922(2)	
V (Å^3)	1676.68(5)	1359.31(17)	1911.6(6)	1924.9(2)	6055.0(10)
Z	4	4	2	2	4
F(000)	592	760	888	920	3048
θ (range)	3.107–29.515°	1.678–25.718°	1.981–27.522°	2.555–27.28°	2.285–27.522°
Max./min. transmission	1.000/0.6042	0.4920/0.2737	0.7456/0.4209	0.0285/0.0064	0.7456/0.3935
Ind refln (R_{int})	4322(1)	2381 (0.0937)	8766 (0.0594)	6686 (0.0917)	13 904 (0.1346)
Final R indices [$I > 2\sigma(I)$]	R_1 = 0.0703, wR_2 = 0.2152	R_1 = 0.0451, wR_2 = 0.1262	R_1 = 0.0408, wR_2 = 0.0774	R_1 = 0.0541, wR_2 = 0.1341	R_1 = 0.0509, wR_2 = 0.1006

PXRD patterns were compared with their experimental ones, confirming their phase purity (Fig. S22–S24, ESI†). As shown in Scheme 1, compounds **1** and **4** are insoluble coordination polymers, while compounds **2** and **3** are molecular coordination compounds and therefore soluble in most organic solvents. All spectroscopic and analytical data is consistent with the solid-state structures determined by single crystal X-ray diffraction methods (*vide infra* and Fig. S25–S32, ESI†)

Crystal structures

Suitable crystals for SCXRD were obtained for all compounds (Table 1). Coordination polymers **1** and **4** crystallized in the monoclinic $P2_1/c$ space group, while molecular compounds **2** and **3** crystallized in the triclinic $P\bar{1}$ space group (Fig. 1–3).

[Cu(L1)I]$_n$ (1). Single crystal analysis of **1** revealed this compound to be a 1D coordination polymer (Fig. 1). **1** forms a 1D zigzag network with each iodine atom bridging two Cu(I) atoms. Each Cu centre is surrounded by a nitrogen atom of the pyrazole ligand and two iodine bridges (Fig. 1a). Thus, the Cu atoms are three-coordinated, giving a trigonal-planar coordination geometry, with an I–Cu–I angle of 113.8°. Selected bond lengths and angles are listed in Table S1 (ESI†). The geometric parameters for this coordination polymer agree with the values found in other Cu(I)–iodine structures.[20] Cu···Cu and I···I distances in the 1D zigzag network are rather long (4.2749(8) and 4.2749(5) Å, respectively) to be considered metallophilic interactions. The closest pyrazole–pyrazole and phenyl–phenyl rings within **1** are oriented in a head-to-head fashion with ring centroid to centroid distances of 4.275 Å, all consistent with the presence of π–π stacking interactions (Fig. 1b). The 1D chains are interacting with one another through intermolecular C_{Pz}–H···π_{Ph} interactions (H···C 2.833 Å, C–H···C 148.9°; see dotted blue lines in Fig. 1c), providing corrugated 2D sheets parallel to the *ab* plane (Fig. 1c). Stacking of the sheets along the *c* axis gives rise to the 3D packing of **1** (Fig. 1c). The 2D sheets interact with one another through intermolecular C_{Ph}–H···I contacts (H···I 3.18 Å, C–H···I 139.2°; see dotted blue lines in Fig. 1c).

[Cu(L2)I]$_2$ (2) and [Cu(L3)I]$_4$ (3). Cu(I) compounds formed from carborane based pyrazole ligands **L2** and **L3** provide molecular compounds **2** and **3**, respectively (Scheme 1). This contrast with the non carborane 2D aromatic ligand **L1**, which formed the coordination polymer **1**. Single crystal analysis of **2** revealed a dinuclear complex with the chemical composition [Cu**L2**I]$_2$. Fig. 2a shows a rhombohedric shaped Cu_2I_2 core featuring very short Cu···Cu distances. There are two independent molecules in the unit cell with slightly different Cu···Cu distances, 2.4728(8) and 2.5158(9) Å. Each trigonal-planar Cu atom of **2** is bonded to the carboranyl pyrazole ligands through the pyrazole N atom. Selected bond lengths and angles are listed in Table S1 (ESI†). The geometric parameters for this complex agree with the values found in other Cu(I)–iodine structures.[94] The Cu_2I_2 unit lies on an inversion center that is located in the middle of the motif. Consequently, the carboranyl pyrazole ligands lie on opposite sides of the plane containing the Cu_2I_2 units. Within each molecule, the pyrazole rings' planes are nearly perpendicular to that of the Cu_2I_2 plane (84.54°). The 3D structure of **2** is formed by self-assembly of molecules by intermolecular C–H···N interactions (H···N 2.717 Å, C–H···N 145.4°; see dotted blue lines in Fig. 2b) between the carborane C–H atoms and a one of the pyrazole nitrogen atoms (Fig. 2b).

The structure of **3** consists of a tetranuclear complex containing a Cu_4I_4 cluster and four molecules of ligand (Fig. 2c). Compound **3** represents a novel example of the rare octahedral clusters (Chart 1).[19] The four Cu(I) atoms are arranged in a rectangular array with two significantly different Cu···Cu distances [2.5917(8) and 2.9289(7) Å]. The **L3** and iodide ligands

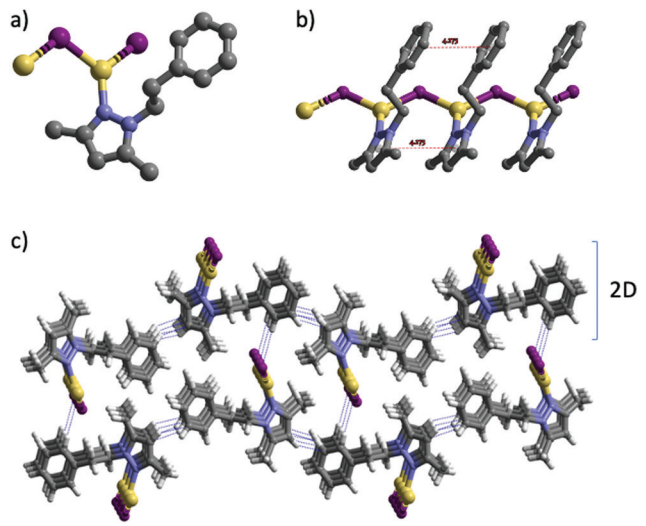

Fig. 1 Crystal structure of **1**: (a) view of the coordination environment of the Cu(I) centers. (b) Fragment of the 1D network of **1** showing the π–π interactions. (c) View of the 3D structure. H atoms have been omitted for clarity in (a) and (b). Intermolecular contacts are shown as dotted blue lines. Color codes: H pale grey; C grey; N blue; I violet; Cu yellow.

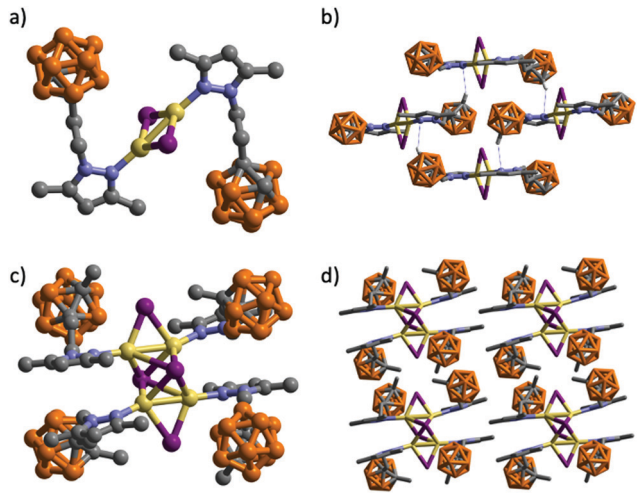

Fig. 2 Molecular structures of **2** (a) and **3** (c) and two perspective views of the packing of four molecules (b) and (d). H atoms have been omitted for clarity. Intermolecular contacts are shown as dotted blue lines. Color codes: B orange; C grey; N blue; I violet; Cu yellow.

bridge each edge of the Cu_4 plane to form a $Cu_4(\mathbf{L3})_4I_4$ core. The Cu_4 plane is further μ_4-capped by two iodine atoms providing a distorted octahedron (Fig. 2c). The Cu–I bond lengths in μ_4-bridging Cu–I lengths vary from 2.6985 to 3.1044 Å, which are significantly longer than the ones bridging the edges of the Cu_4 plane (2.5662 and 2.6475 Å). The carboranyl pyrazole ligands coordinate to the four Cu(I) atoms through the ligand's pyrazole N atom (Fig. 2c). Cu–N distances vary from 1.985(4) to 1.990(4) Å. Selected bond lengths and angles are listed in Table S2 (ESI†). The geometric parameters have been compared with other reported examples. There are only fifteen entries in the CSD[95] for eleven such type of octahedral cluster compounds and all of them bear two bidentate (neutral P^N[25,31,96,97] or anionic N^N[19]) ligands. Thus, complex **3** represents the first example of such a family having monosubstituted neutral N-donor ligands. The 3D structure in this case is formed by self-assembly of molecules by weak intermolecular C–H···I (H···I 3.019 Å, C–H···I 161.7°) and C–H···H–B (H···H 2.448 Å, C–H···H 130.5°, B–H···H 110.4°) contacts (Fig. 2d and Fig. S33, ESI†).

$[Cu_4(L4)_2I_4]_n$ (4). Single crystal analysis of **4** reveals this compound as a 3D coordination polymer (Fig. 3). Each carboranyl bis-pyrazole ligand coordinates to two different Cu_xI_x clusters, namely, a rhombohedric shaped $[Cu_2I_2]$ cluster and a stepped cubane $[Cu_4I_4]$ cluster. The rhombohedric shaped Cu_2I_2 core is similar to that present in complex **2** and features a quite short Cu···Cu distance of 2.588(1) Å. Each trigonal-planar Cu(I) atom in this Cu_2I_2 core is bonded to two different carboranyl bis-pyrazole ligands through the pyrazole N atom. The stepped cubane $[Cu_4I_4]$ cluster can be seen as the deformation of the normal cubane-like $[Cu_4I_4]$ cluster by the cleavage of two *trans*-Cu–I bonds located in the same face of the cubane and bending the free rhombohedra to fulfil the chair conformation. The Cu3···Cu4 distance is 2.637(1) Å, which is quite short implying strong metal···metal bonding interactions. Each stepped cubane core is bonded to four different carboranyl bis-pyrazole ligands through the pyrazole N atom. Selected bond lengths and angles are listed in Table S3 (ESI†). Although these two types of Cu_xI_x clusters have been reported,[18] compound **4** represents the first example where both types are combined in a coordination polymer. The carboranyl pyrazole ligand **L4** adopts two different conformations that alternate along the 3D structure (Fig. S34, ESI†).

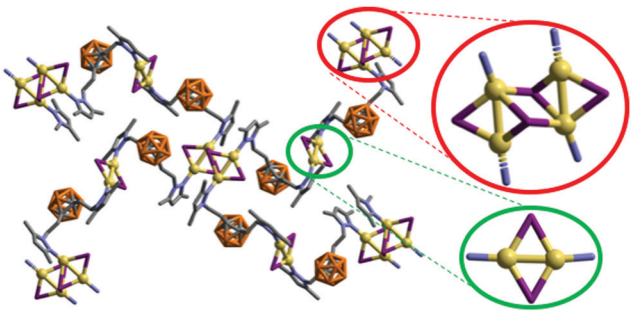

Fig. 3 Fragment of the 3D structure of **4** showing rhombohedric $[Cu_2I_2]$ (green) and stepped cubane $[Cu_4I_4]$ (red) clusters. H atoms have been omitted for clarity. Color codes: B orange; C grey; N blue; I violet; Cu yellow.

It is noteworthy that whilst the pyrazolylphenyl ligand (**L1**, Scheme 1) provides a Cu(I) coordination polymer, the corresponding ligands with carborane in place of phenyl (**L2–L3**, Scheme 1) provide 0D metal compounds (Scheme 1 and Fig. 1, 2). The π–π interactions observed between the pyrazole and phenyl rings of **L1** in compound **1** indicate that most probably such interactions occur in solution and during the reaction with CuI to provide the observed single chain coordination polymer **1**. Such π–π interactions are not possible when the phenyl ring is replaced by the carborane fragments and this obviously prevents the formation of coordination polymers. The latter can only be obtained by employing the disubstituted carboranyl pyrazole ligand **L4** (Scheme 1 and Fig. 3).

Luminescence properties in the solid state

Compounds **1–4** are white crystalline solids under ambient light. The absorption spectra of **1–4** were measured in solid-state at room temperature (Fig. S35, ESI†). Polymer **1** shows three absorption bands at high energies (224, 269, 290 nm) and a shoulder at lower energy (369 nm). Complex **2** exhibits a maximum of absorption at 363 nm. The tetranuclear complex **3** shows three absorption regions, the first one at high energy in the range from 200 nm to 320 nm with a maximum at 306 nm, a second region in the range 320–410 nm and a the third one at lower energy from 410 tailing to 600 nm. Polymer **4** exhibits a very broad absorption band composed of two different regions, the high energy region from 210 nm to 320 nm with two maxima at 257 and 289 nm and a low energy region from 320 nm tailing to 600 nm. This broad absorption band of **4** seems to correspond to the combined absorption spectra for **2** and **3** (Fig. S35, ESI†). Absorption bands at higher energies have been associated with pyrazole ligand-centred $\pi \rightarrow \pi^*$ transitions, and they correlate nicely with the UV-vis spectra of the free ligands (Fig. S16, ESI†). On the other hand, lower energy absorptions have been attributed to (X+M)LCT transfers.[98] In order to further investigate the UV-vis spectra, theoretical calculations were performed for discrete coordination compounds **2** and **3** (*vide infra*).

The normalised solid-state excitation and emission spectra for the four compounds are shown in Fig. 4. The emissive excited states observed in Cu(I)–halide compounds are known to originate from a variety of sources, such as halide-to-ligand charge transfer (XLCT),[1,99] metal-to-ligand charge transfer (MLCT),[1,99] intra-ligand charge transfer (ILCT),[100] and, for Cu(I)-cluster compounds, a cluster-centred excited state of d–s character (CC).[99] As such, their photophysical properties bear a strong intrinsic relationship with their structural features.

The crystalline solid of polymer **1** exhibits dual emission in the blue (460 nm, HE) and orange (609 nm, LE) regions of the visible spectra upon excitation at 283 nm, with low absolute quantum yield (Φ_F) of 4% (Table 2). The emission spectrum of **1** is broad and unstructured, which according to the literature on Cu(I) compounds is typical of charge-transfer (CT) emissions.[101]

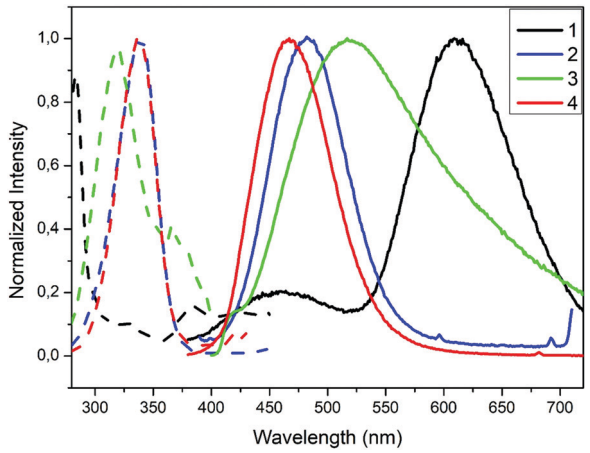

Fig. 4 Excitation (dashed lines) and emission (solid lines) spectra for compounds **1–4** in the solid state at 298 K.

Table 2 Photophysical data for compounds **1–4**

Compound	UV-vis maximum absorbance (nm)	Excitation (λ_{max}, nm)	Emission (λ_{max}, nm)	Φ_F (%)
1	290	283	460, 609	3.8
2	363	340	483	66.5
3	306	318	517	4.9
4	349	336	467	13.7

Contrary to Cu(I)–iodide rhomboid dimers or tetramers, photophysical studies of single-stranded Cu(I)–iodide polymers are scarce. The first one was reported by Cariati *et al.* in 2002,[3] and since, only few others have been reported.[48,49,102,103] As the Cu–Cu bond length is the primary factor governing CC excited states in Cu(I) clusters,[4] their long distances in **1** (4.275 Å, Table S4, ESI†), being larger than the sum of their van der Waals radii (2.8 Å), seem to preclude them as the source of its emission. Thus, according to the few reports on similar single-stranded Cu(I) polymers, the HE emission is attributed to a mixture of ^{3}XLCT and ^{3}MLCT,[48,49,102] whereas LE emission to ^{3}XMCT.[104] Note that there are only two cases of double emission in single-stranded Cu(I) polymers, both reported by Cariati.[3] Although similar results have been reported for double-stranded or grid-like Cu(I) polymers,[105,106] direct extrapolation should be avoided, as the latter can possess ^{3}CC based-emission[104,107] and they show completely different structures. The remarkable Stokes shift for polymer **1** is striking in comparison with the other three compounds (Table 2). Such large shifts have been explained in 2D grid-like $[CuBr(pyz)]_n$ (pyz = pyrazine) and $[CuBr(quinz)]_n$ (quinz = quinazoline) compounds by a HOMO (based on a mix of halide 4p and metal 3d orbitals) to an antibonding LUMO (ligand based) charge transfer ((X + M)LCT).[108] Charge transfer to an antibonding LUMO should cause a geometrical change in the bonds, resulting in a large Stokes shift. This fact is also consistent with the low measured quantum efficiency value for **1**.

Molecular compounds **2–3** emit at high energies, in the pblue-to-yellow region (450–520 nm) of the visible spectrum (Fig. 4 and Table 2). A crystalline powder of complex **2** exhibits an outstanding blue emission compared to other analogues,[103] with a maximum at 483 nm upon excitation at 340 nm, and an absolute quantum yield (Φ_F) of 66.5%. The emission spectrum is also broad and unstructured, consistent with charge-transfer emissions.[109] Among the reported Cu(I) rhomboid dimers, the majority corresponds to four coordinated Cu(I)-dimers, with only *ca.* 20% of the structures being three-coordinated Cu(I) compounds (such as in **2**).[110,111] Thus, photophysical properties of the tetra-coordinated Cu-dimers have been extensively studied; in particular the rhomboid dimers containing bidentate $N_{pyridine}$,P-heteroleptic ligands have been extensively studied by Bräse's group.[7,13,24,109,112] Their analyses have revealed that HOMO orbitals are mainly centred in the Cu_2X_2 framework and LUMO orbitals in the pyridine ligand. Thus, their emission stems mainly from (X + M)LCT, and can be tuned by slightly modifying the pyridine ligands.[13,24,109,112] As mentioned above, dimeric Cu(I) compounds with tri-coordinated metal centres, such as **2**, are much less studied than the corresponding tetra-coordinated compounds. Thus, the few reports in tri-coordinated compounds assume a similar origin for their emission than the tetra-coordinated one.[113–115] We therefore decided to perform TDDFT calculations in order to verify or refute this hypothesis (*vide infra*). To the best of our knowledge, ours is the first report of photophysical studies of N-donor tri-coordinated Cu(I) rhomboid dimer compounds supported by TDDFT calculations.

The crystalline solid of complex **3** shows a very broad emission band with a maximum at 517 nm upon excitation at 318 nm at room temperature with an absolute Φ_F of around 5% (Fig. 4 and Table 2). The latter is significantly lower than those reported for a number of homologous compounds.[26,28] For some reported octahedral Cu_4I_4 compounds, dual emission has been observed, that is a LE emission (550–600 nm) dominating at room temperature and a HE emission (400–500 nm) dominating at lower temperatures.[23,28,31] By analogy with the better studied $Cu_4I_4L_x$ (x = 2–4) cubane clusters, these have been attributed to ^{3}CC transitions and ^{3}XLCT transitions respectively.[25,26,29] However, recent studies have shown that other octahedral clusters display single LE or HE emission bands which are largely temperature independent,[116,117] a phenomenon known as rigidochromism, while others display only a single emission in the region of 500–560 nm, halfway between LE and HE emission.[28,30] Complex **3** seems to fall under this behaviour, as no dual emission is observed. This disparity in the results of photophysical studies for octahedral clusters show that a universally accepted process for rationalizing its photoluminescent behaviour has yet to been achieved. Therefore, we have performed the TD-DFT calculations for **3** (*vide infra*).

The crystalline solid of multinuclear coordination polymer **4** exhibits blue emission with a maximum at 467 nm upon excitation at 336 nm and an absolute quantum yield of 13.7% (Fig. 4 and Table 2). It is noteworthy that both the emission and excitation spectra of **4** are similar to those of complex **2** (Cu_2I_2 units). In one of the few Cu(I) compounds containing different

metal clusters, it was observed that its photoluminescent behaviour was a combination of that of its constituent parts.[44] Thus, assuming a similar behaviour for **4**, it seems that the emission originating in the Cu_2I_2 unit dominates over that originating in the open cubane Cu_4I_4 unit. This fact is also consistent with the high Φ_F observed for **2**, compared to the low Φ_F observed for the tetranuclear cluster in **3**. Thus, we assume the emission for both **4** and **2** originate in the dimeric units. On this basis, the TDDFT calculations performed for **2** also help shed some light on the photophysical results obtained for **4** (*vide infra*).

In order to analyze and fully understand the photophysical properties of the molecular systems, time-dependent density functional theory (TDDFT) calculations (see Computational details section) were performed using Gaussian16 program,[118] with the B3LYP functional[119,120] using the Def2TZV basis set.[121] Complex **2**, containing a rhombohedral shape Cu_2I_2 core, has absorption and excitation peaks at 363 and 340 nm, respectively (Table 2). The calculated TDDFT values at B3LYP level show the first non-zero extinction coefficient (second excitation) at 321 and 335 nm, respectively for the optimized and experimental structures. The orbitals involved in such processes are represented in the top of Fig. 5. The excitation is from the HOMO to the LUMO+1, and it can be described as a (X + M)LCT transfer from the Cu_2I_2 framework to the ligand, much in the same manner as the tetracoordinated rhomboid dimers studied by Bräse's group.[13,24,109,112] Previously, it has been reported that the deexcitation in these kinds of systems are through triplet states with long excited state lifetimes.[122] The theoretical analysis of the emission spectra was done by optimizing the structure of the wavefunction corresponding to the triplet state (see Experimental section for details). The structure of the triplet excited state from **2** is very distorted with non-bridging iodide ligands (see Fig. 5), as already reported for other Cu_2I_2 systems.[122] The Cu···Cu distance was found to be 2.346 and 2.593 Å in the optimized triplet excited and singlet ground state, respectively, and 2.516 Å in the experimental structure. The results indicate that the emission is from the LUMO orbital to HOMO−1 and HOMO−2 (see Fig. 5 bottom). There are triplet excitations (542, 498 and 487 nm) that are close to the experimental emission peak (483 nm). The analysis of the orbitals involved in such deexcitation transitions reveals that they basically occur among the Cu_2I_2 orbitals. The LUMO is mainly a combination of 4s copper orbitals while HOMO−1 and HOMO−2 correspond to bonding d–d orbitals (for $d_{x^2-y^2}$ and d_{z^2} pairs) of copper mixed with large contributions of p orbitals of the iodine atoms. Thus, such deexcitation transitions could be described as cluster-centred excited state of d–s transition in origin, therefore contradicting the previous reports that hypothesized that they were (X + M)LCT in origin.[113–115] A similar result was observed for an adduct containing Cu_2I_2 and Cu_3-pyrazolate clusters.[122] Those results suggest that tetra-coordinated and tri-coordinated Cu_2I_2 clusters follow different emission behaviour.

In the case of complex **3**, there are four calculated excitations that have non-zero extinction coefficients in the same region as the experimental results. They correspond to transitions between a mixture of the three last occupied orbitals (HOMO, HOMO−1 and HOMO−2, Fig. 6 top) with large contribution of iodine and copper atoms to the first empty orbitals (LUMO, LUMO+1, LUMO+2 and LUMO+3, Fig. 6 bottom), which are mainly ligand-based. The calculated excitation values are 310, 305, 301, 295 nm for the experimental structure (second, third, sixth and seventh excitations) while for the optimized structure are 318, 312, 305 and 298 nm (first, third, fifth and seventh excitations). Such values are in good agreement with the experimental absorption and excitation peaks of 306 and 318 nm, respectively. The nature of such excitation is clearly a (X + M)LCT transfer from the Cu_4I_4 framework.

One of the most appealing features of the photophysical properties of **3** is the very large Stokes shift with an emission at 517 nm (Table 2). In order to analyse the origin of such a large shift in the emission, we have optimized the structure of the excited states of this molecule. The optimization of such state leads to a huge change in the structure of the Cu_4I_4 framework (see Fig. 7). As we have previously seen for **2**, the structure is considerably distorted, especially the central Cu_4I_4 framework. One of the Cu_2I_2 units adopts a similar structure to that of the

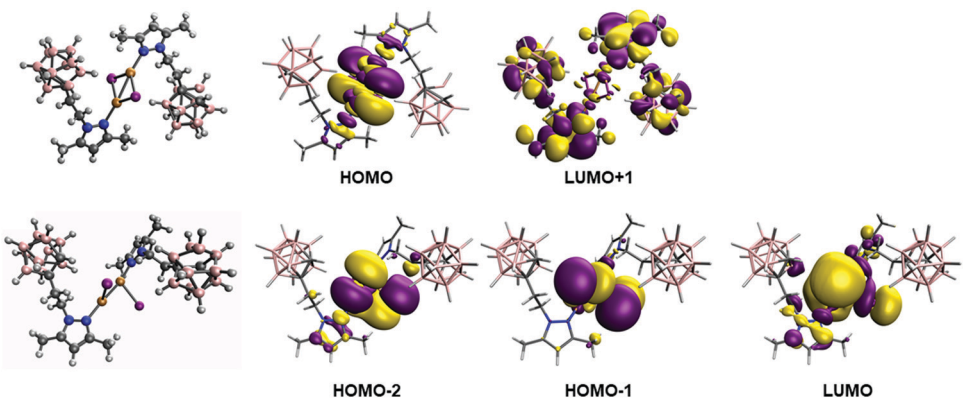

Fig. 5 Top: Ground state structure and calculated orbitals at B3LYP level involved in the absorption process for **2**. Bottom: Optimized structure of triplet state involved in the deexcitation process and the orbitals of the singlet state with such optimized structure.

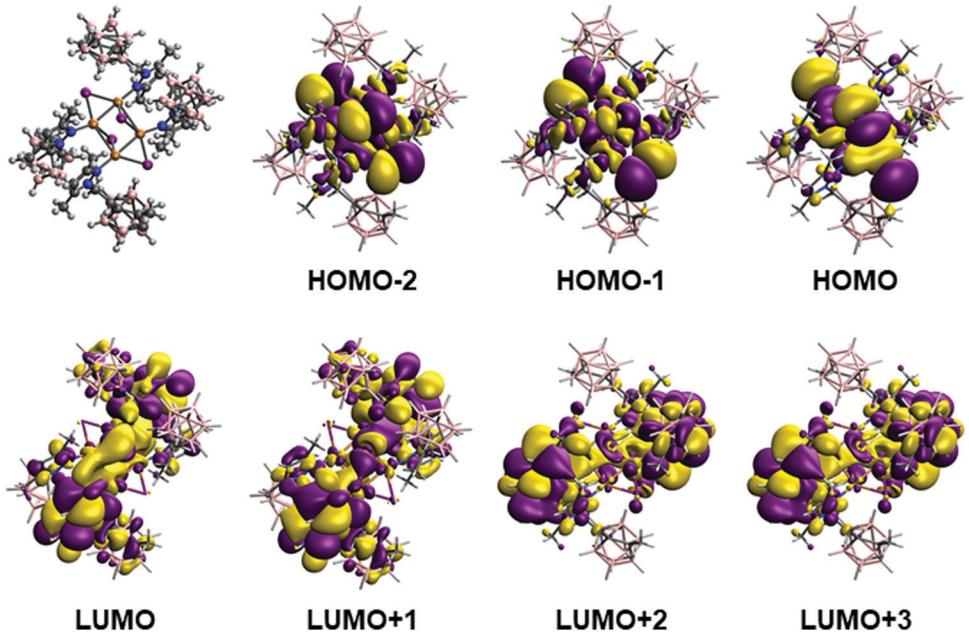

Fig. 6 Optimized structure and calculated orbitals at B3LYP level involved in the absorption process that corresponds to transition between a mixture of the three last occupied orbitals to the first empty orbitals for complex **3**. See the text for details.

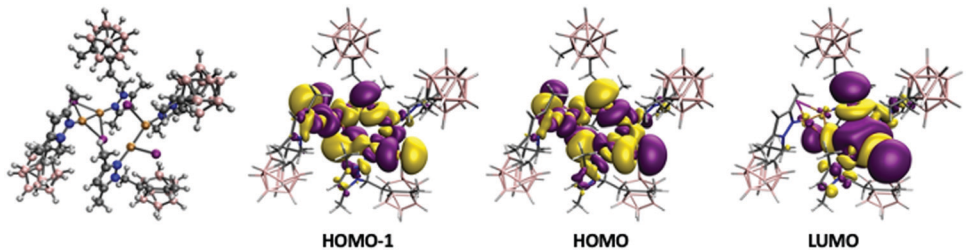

Fig. 7 Optimized structure of triplet state of **3** involved in the deexcitation process and the orbitals of the singlet state with such optimized structure. See the text for details.

triplet state of complex **2** with a short Cu–Cu distance (2.363 Å) and with terminal iodide ligands (see Fig. 5 and 7). The second Cu_2I_2 moiety has the bridging iodide ligands and a relatively long Cu···Cu distance (2.655 Å). The calculation of the vertical excitations using TDDFT of the singlet ground state for such triplet optimized structure gives triplet deexcitation transitions at 538 and 531 nm in good agreement with the experimental emission band at 517 nm. The analysis of the orbitals involved indicates a deexcitation from the LUMO orbital (Fig. 7) mainly localized in the Cu_2I_2 moiety with short Cu···Cu distance to orbitals delocalized in the whole Cu_4I_4 framework (HOMO and HOMO−1, Fig. 7). Thus, as for **2**, the deexcitation process can be described as a ^{3}CC process.

Conclusions

In summary, we have synthesized and fully characterized two monosubstituted carboranyl pyrazole ligands (**L2** and **L3**) and one disubstituted carboranyl pyrazole ligand (**L4**) by lithiation and nucleophilic addition onto the corresponding 3,5-dimethyl-1-(2-toluene-*p*-sulfonyloxyethyl)pyrazole. All new ligands, and the corresponding monosubstituted phenyl derivative (**L1**) behave as N-type ligands upon coordination with CuI to afford a series of polymeric ($[Cu(\mathbf{L1})I]_n$ (**1**) and $[Cu_4(\mathbf{L4})_2I_4]_n$ (**4**)) or molecular ($[Cu(\mathbf{L2})I]_2$ (**2**) and $[Cu(\mathbf{L3})I]_4$ (**3**)) Cu(I) structures. Whereas **1**, having a phenyl-based pyrazole, forms a coordination polymer, **2** and **3**, both possessing a carboranyl-based pyrazole ligand, form molecular compounds. Lastly, the use of bidentate **L4**, results in the formation of another coordination polymer **4**. **3** represents a novel example of the rare octahedral clusters, and the first one bearing a neutral monodentate ligand. **4** represents the first example where both dimeric and stepped cubane clusters are combined in a single coordination polymer.

Absorption and emission properties of **1–4** have been studied in the solid state. Their emission covers a remarkable range of the visible spectrum, from the blue to the orange (460–609 nm). Noticeably, complex **2** exhibits an outstanding fluorescence efficiency of 66.5%, which is higher than that

observed for reported analogues without the carborane units. TDDFT calculations performed for **2** and **3** allowed us to gain insight in the origin of their emission. For **2**, they confirm that the emission origin is a cluster-centred excited state of d–s transition. This result is remarkable, as, to date, the origin of the emission in similar dimers has been assumed to be (X + M)LCT in nature. Regarding compound **3**, TDDFT calculations indicate that the emission is through a ^{3}CC state. Calculations also show that, upon excitation, **3** suffers a notable distortion resulting in the total cleavage of the Cu_4I_4 framework. To the best of our knowledge, this is the first time that such behaviour is observed for this type of octahedral compounds. These results depart from the classical assumption that octahedral Cu_4I_4 clusters behave as cubane clusters, highlighting that more effort is required to rationalise their emission.

We demonstrate that it is possible to tune the molecular structure and luminescence properties of these Cu(I) compounds by changing a phenyl ring (2D) by a carborane cluster (3D), which also allows introducing substituents at the cage. Herein, we report new understanding on some significant luminescence aspects for a rare type of Cu(I) complex for the first time and explore the relationship between the structural features and their luminescent behaviour, a knowledge that is key in the rational design of photoluminescent materials.

Experimental section

Materials and methods

All synthetic procedures were performed under dinitrogen atmosphere using standard Schlenk techniques unless otherwise noted. Tetrahydrofuran (THF) was purchased from Carlo Erba Reagents S.A. and distilled from Na/benzophenone prior to use. Commercial grade acetonitrile (CH_3CN) was purchased from Merck and dried using 3 Å activated molecular sieves under dinitrogen atmosphere for 48 h. Spectroscopic grade methanol (MeOH) was purchased from ROMIL-SpS and used without further purification. 3,5-Dimethyl-1-(2-toluene-*p*-sulfonyloxyethyl)pyrazole was synthesized according to reported procedures.[123] Ligand **L1** and all other chemicals were commercially available and used as received.

Synthesis of carboranyl pyrazole ligands L2 and L4. *n*-BuLi (4.70 ml, 1.50 M in hexane, 7.05 mmol) was added dropwise to a solution of *o*-carborane (0.456 g, 3.16 mmol) in dry THF (20 mL) under a nitrogen atmosphere at 0 °C (ice/water bath). The solution was stirred for 45 minutes at 0 °C and 45 minutes at r.t. resulting in a pale-yellow suspension. Next, a solution of 3,5-dimethyl-1-(2-toluene-*p*-sulfonyloxyethyl)pyrazole (1.696 g, 6.33 mmol) in dry THF (20 mL) under an inert atmosphere was carefully cannulated over the lithiate at 0 °C (ice/water bath). The mixture was stirred overnight under an inert atmosphere, letting it warm naturally to r.t. The mixture was then quenched using a saturate aqueous solution of NH_4Cl (10 mL). The aqueous phase was extracted using $CHCl_3$ (3 × 20 mL) and the organic layers were dried over anhydrous $MgSO_4$. The desired products were purified by preparative TLC (**L2**, eluent = ethyl acetate/chloroform 1 : 4, R_f = 0.76; L4, eluent = ethyl acetate/hexane 9 : 1, R_f = 0.68). The products were extracted from the corresponding silica portions with $CHCl_3$ and obtained as white powders on solvent evaporation. The products were washed with cold hexane (2 mL) and dried under vacuum.

L2. Yield: 33% (0.622 g). Elem. anal. calc. for $C_9H_{22}B_{10}N_2$ (266.39): C 40.58, H 8.32, N 14.01. Found: C 40.49, H 8.23, N 13.85. M.p.: 172–176 °C. ATR-FTIR (wavenumber, cm^{-1}): 2982–2917 (w) [ν(C–H)$_{al}$], 2561 (s) [ν(B–H)], 2551 (s) [ν(B–H)], 1555 (s) [ν(C=C/C=N)$_{ar}$], 1489 (w), 1466 (m), 1442 (m), 1425 (s) [δ(C=C)/δ(C=N)$_{ar}$], 1377 (w), 1372 (m), 1321 (m), 1282 (w), 1218 (w), 1139 (w), 1071 (m), 1024 (s) [δ(C–H)$_{ip}$], 988 (w), 937 (w), 903 (w), 835 (w), 789 (vs) [δ(C–H)$_{oop}$], 719 (vs) [δ(C–H)$_{oop}$], 673 (w), 656 (w), 640 (w), 556 (w), 540 (w). ^{1}H NMR (CD_3CN, 400.0 MHz): δ = 5.84 (s, 1H, C*H*(Pz)), 4.43 (br, 1H, C_{carb}–H) 4.06 (m, 2H, $N_{Pz}CH_2CH_2C_{carb}$), 2.75 (m, 2H, $N_{Pz}CH_2CH_2C_{carb}$), 2.19 (s, 3H, Pz-CH_3), 2.10 (s, 3H, Pz-CH_3). ^{11}B NMR (CD_3CN, 128.6 MHz) δ = −2.75 (br d, $^1J_{BH}$ = 155.0, 1B), −5.67 (br d, $^1J_{BH}$ = 155.0, 1B), −9.66 (br d, $^1J_{BH}$ = 149.5, 2B), −10.2 to −13.6, overlapping signals (6B). ^{11}B{^{1}H} NMR (CD_3CN, 128.6 MHz) δ = −2.88 (br s, 1B), −5.75 (br s, 1B), −9.65 (s, 2B), −11.15 to −13.0, overlapping signals (6B). ^{13}C{^{1}H} NMR (CD_3CN, 100.6 MHz): δ = 147.6, 145.5 (Pz-*C*), 108.1 (Pz-*CH*), 73.0 (C_{carb}–CH_2R), 63.7 (C_{carb}–H), 47.3 (C_{carb}–$CH_2CH_2N_{Pz}$), 36.5 (C_{carb}–$CH_2CH_2N_{Pz}$), 11.8, 11.2 (CH_3(Pz)). UV-vis: (CH_3CN, 6.5 × 10^{-5} M) λ_{max} (ε (M^{-1} cm^{-1})) = 201 nm (6380).

L4. Yield: 13% (0.184 g). Elem. anal. calc. for $C_{16}H_{32}B_{10}N_4$ (388.56): C 49.46, H 8.30, N 14.01. Found: C 49.32, H 8.17, N 13.92. M.p.: 100–115 °C. ATR-FTIR (wavenumber, cm^{-1}): 3128 (w) [ν(C–H)$_{ar}$], 2996–2856 (w) [ν(C–H)$_{al}$], 2563 (br, vs) [ν(B–H)], 1552 (s) [ν(C=C/C=N)$_{ar}$], 1450 (s), 1416 (s) [δ(C=C)/δ(C=N)$_{ar}$], 1383 (s), 1365(s), 1315(s), 1258 (s), 1213 (m), 1173 (w), 1135 (w), 1080 (w), 1062 (w), 1020 (m), 981 (m), 980 (m), 788 (vs) [δ(C–H)$_{oop}$], 717 (vs) [δ(C–H)$_{oop}$], 670 (vs) [δ(C–H)$_{oop}$], 632 (m), 534 (m).^{1}H NMR (CD_3CN, 400.0 MHz): δ = 5.78 (s, 2H, C*H*(Pz)), 4.09 (m, 4H, $N_{Pz}CH_2CH_2C_{carb}$), 2.79 (m, 4H, $N_{Pz}CH_2CH_2C_{carb}$), 2.21 (s, 12H, CH_3(Pz)). ^{11}B NMR (CD_3CN, 128.6 MHz): δ = −4.71 (br d, $^1J_{BH}$ = 149.4, 1B), −9.64 to −11.64, overlapping signals (8B). ^{11}B{^{1}H} RMN (CD_3CN, 128.6 MHz): δ = −4.71 (br s, 2B), −10.2 and −11.1 overlapping signals (8B). ^{13}C{^{1}H} NMR (CD_3CN, 100.6 MHz): δ = 147.3 and 139.3 (Pz-*C*), 106.0 (*CH*(Pz)), 78.0 (C_{carb}), 46.6 ($N_{Pz}CH_2CH_2C_{carb}$), 33.9 ($N_{Pz}CH_2CH_2C_{carb}$), 12.5 and 10.0 (CH_3(Pz)). UV-vis: (CH_3CN, 5.2 × 10^{-5} M) λ_{max} (ε (M^{-1} cm^{-1})) = 214 nm (6231).

Synthesis of carboranyl pyrazole ligand L3. A similar procedure as that described above was followed: *n*-BuLi (2.70 mL, 1.50 M in hexane, 4.05 mmol), 1-methyl-*o*-carborane (0.834 g, 3.270 mmol) in dry THF (20 mL) and 3,5-dimethyl-1-(2-toluene-*p*-sulfonyloxyethyl)pyrazole (1.002 g, 3.74 mmol) in dry THF (20 mL). After quenching the reaction by using a saturated aqueous solution of NH_4Cl (10 mL), the aqueous phase was extracted using Et_2O (3 × 20 mL) and the organic layers were

dried over anhydrous $MgSO_4$. **L3** was purified by preparative TLC (eluent = ethyl acetate/hexane 2 : 3, R_f = 0.47). The product was extracted from the corresponding silica portions with THF and obtained as white powders on solvent evaporation. Crystals suitable for SCXRD were obtained *via* slow evaporation of the latter THF solutions.

L3. Yield: 36% (0.326 g). Elem. anal. calc. for $C_{10}H_{24}B_{10}N_2$ (280.42): C 42.83, H 8.63, N 9.99. Found: C 42.59, H 8.33, N 9.69. M.p.: 138–142 °C. ATR-FTIR (wavenumber, cm^{-1}): 3134–3061 (w) [ν(C–H)$_{ar}$], 2978–2858 (w) [ν(C–H)$_{al}$], 2571 (s) [ν(B–H)], 1554 (s) [ν(C═C/C═N)$_{ar}$], 1482 (w), 1463 (m), 1452 (s) [δ(C═C)/δ(C═N)$_{ar}$], 1421 (s), 1388 (s), 1372 (w), 1317 (w), 1299 (w), 1278 (m), 1218 (w), 1177 (w), 1161 (w), 1129 (w), 1088 (w), δ(C–H)$_{ip}$: 1024 (s), 977 (w), 946 (w), 921 (w), 779 (s) [δ(C–H)$_{oop}$], 726 (s) [δ(C–H)$_{oop}$], 666 (m), 648 (m), 550 (m). ^{1}H NMR (CD_3CN, 400.0 MHz): δ = 5.78 (s, 1H, C*H*(Pz)), 4.07 (m, 2H, $N_{Pz}CH_2CH_2C_{carb}$), 2.72 (m, 2H, $N_{Pz}CH_2CH_2C_{carb}$), 2.21 (s, 3H, CH_3(Carb)), 2.10 and 2.08 (s, 6H, CH_3(Pz)). ^{11}B NMR ($CDCl_3$, 128.6 MHz): δ = −4.42 (br d, $^1J_{BH}$ = 157.3 Hz, 1B), −6.08 (br d, $^1J_{BH}$ = 151, 1B), −8.28 to −11.40, overlapping signals (8B). ^{11}B{^{1}H} NMR (CD_3CN, 128.6 MHz): δ = −4.4 (br s, 1B), −6.2 (br s, 1B), −8.9 to −10.8, overlapping signals (8B). ^{13}C{^{1}H} NMR (CD_3CN, 100.6 MHz): δ = 148.2 and 140.1 (Pz-*C*), 106.9 (*CH*(Pz)), 47.7 ($N_{Pz}CH_2CH_2C_{carb}$), 36.1 ($N_{Pz}CH_2CH_2C_{carb}$), 23.6 (CH_3(Carb)), 13.6 and 11.1 (CH_3(Pz)). UV-vis: (CH_3CN, 2.1 × 10^{-5} M) λ_{max} (ε (M^{-1} cm^{-1})) = 196 nm (1012).

Synthesis of [Cu(L1)I]$_n$ (1). A solution of anhydrous CuI (0.019 g, 0.098 mmol) and **L1** (0.020 g, 0.098 mmol) in dry CH_3CN (20 mL) was stirred at r.t. until all CuI was dissolved. After that period, the solvent was evaporated under vacuum, resulting in pure **1** as a white powder. Suitable crystals for SCXRD were obtained *via* slow evaporation of the solvent.

1. Yield: 60.1% (0.023 g) elem. anal. calc. for $C_{13}H_{16}IN_2Cu$ (390.72): C 39.96, H 4.13, N 7.17. Found: C 39.83, H 4.10, N 7.14. ATR-FTIR (wavenumber, cm^{-1}): 3126–3030 (w) [ν(C–H)$_{ar}$], 2978–2855 (w) [ν(C–H)$_{al}$], 1550 (s) [ν(C═C/C═N)$_{ar}$], 1496 (m), 1488 (m), 1462 (m), 1453 (s) [δ(C═C)/δ(C═N)$_{ar}$], 1421 (w), 1388 (m), 1371 (w), 1357 (m), 1310 (m), 1253 (m), 1152 (w), 1075 (w), 1048 (w), 1031 (w), 904 (w), 800 (s), 746 (s) [δ(C–H)$_{oop}$], 696 (s) [δ(C–H)$_{oop}$] and 687 (s) [δ(C–H)$_{oop}$]. UV-vis: (solid state) λ_{max} = 290 nm. Fluorescence (solid state): λ_{ex} = 283 nm, λ_{em} = 609 nm.

Synthesis of [Cu(L2)I]$_2$ (2). A solution of anhydrous CuI (0.127 g, 0.640 mmol) and **L2** (0.0170 g, 0.640 mmol) in dry CH_3CN (20 mL) was stirred at r.t. overnight. Then, the resulting solution was filtered, concentrated up to 5 mL and left standing overnight in the fridge, which provided a white precipitate. The precipitate was filtered, washed with cold Et_2O and dried under vacuum.

2. Yield: 88.6% (0.259 g) elem anal. calc. for $C_{18}H_{44}B_{20}I_2N_4Cu_2$ (913.69): C 23.66, H 4.85, N 6.13. Found: C 23.88, H 4.97, N 6.10. ATR-FTIR (wavenumber, cm^{-1}): 3034 (w) [ν(C–H)$_{ar}$], 2986–2913 (w) [ν(C–H)$_{al}$], 2574 (vs) [ν(B–H)], 1555 (s) [ν(C═C/C═N)$_{ar}$], 1466 (m) [δ(C═C)/δ(C═N)$_{ar}$], 1445 (m), 1421 (w), 1392 (m), 1377 (m), 1319 (m), 1283 (m), 1215 (w), 1136 (w), 1119 (m), 1075 (s), 1049 (m), 1032 (m), 1016 (m), 997 (w), 932 (w), 916 (w), 877 (w), 839 (w), 794 (vs) [δ(C–H)$_{oop}$], 722 (vs) [δ(C–H)$_{oop}$], 697 (w), 674 (w), 656 (m), 582 (w), 561 (w) and 541 (w). ^{1}H NMR (CD_3CN, 400.0 MHz): δ = 5.82 (s, 1H, C*H*(Pz)), 4.47 (br s, 1H, C_{carb}–H) 4.13 (m, 2H, $N_{Pz}CH_2CH_2C_{carb}$), 2.76 (m, 2H, $N_{Pz}CH_2CH_2C_{carb}$), 2.19 (s, 3H, Pz-CH_3), 2.16 (s, 3H, Pz-CH_3). ^{11}B NMR (CD_3CN, 128.6 MHz) δ = −2.86 (br d, $^1J_{BH}$ = 146, 1B), −5.72 (br d, $^1J_{BH}$ = 146, 1B), −9.7 (br d, $^1J_{BH}$ = 158.9, 2B), −10.9 to −13.7, overlapping signals (6B). ^{11}B{^{1}H} NMR (CD_3CN, 128.6 MHz) δ = −2.9 (br s, 1B), −5.80 (br s, 1B), −9.7 (br s, 2B), −11.5 (br s, 2B), −12.1 (br s, 2B), −13.0 (br s, 2B). ^{13}C{^{1}H} NMR (CD_3CN, 100.6 MHz): δ = 148.6, 140.7 (Pz-*C*), 106.3 (Pz-*CH*), 74.2 (C_{carb}–CH_2R), 63.6 (C_{carb}–H), 47.6 (C_{carb}–$CH_2CH_2N_{Pz}$), 37.2 (C_{carb}–$CH_2CH_2N_{Pz}$), 13.8, 11.0 (CH_3(Pz)). UV-vis: (solid state) λ_{max} = 363 nm. Fluorescence (solid state): λ_{ex} = 340 nm, λ_{em} = 483 nm.

Synthesis of [Cu(L3)I]$_4$ (3). A solution of anhydrous CuI (0.037 g, 0.188 mmol) and **L3** (0.051 g, 0.188 mmol) in dry CH_3CN (20 ml) was stirred for 1 h at r.t. under nitrogen. After that period, the solvent was evaporated under nitrogen, resulting in a white powder.

Suitable crystals for SCXRD were obtained *via* recrystallization of a solution of the white powder in dry CH_3CN.

Yield: 58.5% (0.052 g) elem. anal. calc. for $C_{40}H_{96}B_{40}N_8I_4Cu_4$ (1883.48): C, 25.51; H, 5.14; N, 5.95. Found: C, 25.21; H, 4.98; N 5.85. ATR-FTIR (wavenumber, cm^{-1}): 2984–2917 (w) [ν(C–H)$_{al}$], 2563 (s) [ν(B–H)], 1556 (s) [ν(C═C/C═N)$_{ar}$], 1467(w), 1445 (s), 1418 (s) [δ(C═C/C═N)$_{ar}$], 1376 (m), 1324 (m), 1280 (m), 1041 (m), 1023 (m), 779 (s) [δ(C–H)$_{oop}$], 729 (s) [δ(C–H)$_{oop}$], 676 (w), 663 (w), 647 (w) and 633 (w). ^{1}H NMR (CD_3CN, 400.0 MHz): δ = 5.82 (s, 1H, C*H*(Pz)), 4.18 (m, 2H, $N_{Pz}CH_2CH_2C_{carb}$), 2.71 (m, 2H, $N_{Pz}CH_2CH_2C_{carb}$), 2.22 (s, 3H, CH_3(Pz)), 2.15 (s, 3H, CH_3(Pz)), 2.10 (s, 3H, CH_3(Carb)). ^{11}B NMR (CD_3CN, 128.6 MHz): δ = −4.46 (br d, $^1J_{BH}$ = 185, 1B), −6.05 (br d, $^1J_{BH}$ = 143 Hz, 1B), −8.68 (br d, $^1J_{BH}$ = 143, 2B), −9.48 to −11.98 overlapping signals, (6B, *B*-H). ^{11}B{^{1}H} NMR (CD_3CN, 128.6 MHz): δ = −4.40 (br s, 1B), −6.10 (br s, 1B), −8.90 to −10.8, overlapping signals (8B). ^{13}C{^{1}H} NMR (CD_3CN, 100.6 MHz): δ = 148.6 and 140.6 (Pz-*C*), 106.2 (*CH*(Pz)), 77.4 and 76.8 (C_{carb}-CR), 47.7 ($N_{Pz}CH_2CH_2C_{carb}$), 35.0 ($N_{Pz}CH_2CH_2C_{carb}$), 23.7 (CH_3C_{carb}), 13.7 and 11.0 (CH_3(Pz)). UV-vis: (solid state) λ_{max} = 306 nm. Fluorescence (solid state): λ_{ex} = 318 nm, λ_{em} = 517 nm.

Synthesis of {[Cu$_4$(L4)$_2$I$_4$]·(CH$_3$CN)}$_n$ (4). A solution of anhydrous CuI (0.100 g, 0.525 mmol) and **L4** (0.082 g, 0.210 mmol) in dry CH_3CN (20 mL) was stirred for 3 h at r.t. Then, the resulting solution was filtered, concentrated up to 5 mL and left standing overnight in the fridge, which provided a white precipitate. The precipitate was filtered, washed with cold Et_2O and dried under vacuum.

4. Yield: 42.1% (0.068 g) elem. anal. calc. for $C_{34}H_{67}B_{20}N_9I_4Cu_4$ (1538.92): C, 25.85 H, 4.27; N, 7.98. Found: C, 25.67; H, 4.19; N 7.86. ATR-FTIR (wavenumber, cm^{-1}): 3132 (w) [ν(C–H)$_{ar}$], 2990–2918 (w) [ν(C–H)$_{al}$], 2572 (vs)

[ν(B–H)], 1555 (s) [ν(C═C/C═N)$_{ar}$], 1464 (m), 1436 (m), 1417 (s) [δ(C═C/C═N)$_{ar}$], 1376 (s), 1317 (m), 1285 (w), 1248 (m), 1219 (w), 1154 (w), 1113 (w), 1071 (w), 1066 (w), 1036 (s), 998 (m), 982 (m), 798 (vs) [δ(C–H)$_{oop}$], 795 (vs) [δ(C–H)$_{oop}$], 730 (s) [δ(C–H)$_{oop}$], 672 (s), 660 (s), 544 (m), 526 (m). UV-vis: (solid state) λ_{max} = 349 nm. Fluorescence (solid state): λ_{ex} = 336 nm, λ_{em} = 467 nm.

Powder X-ray diffraction patterns (PXRD) for **1–3** were measured using a Siemens D5000 apparatus (with 40 kW and 45 mA using Cu K$_\alpha$ radiation with λ = 1.5406 Å). Patterns were recorded from $2\theta = 5^\circ$ to 40° with a step scan of 0.02° counting for 1 s at each step. For **4**, PXRD pattern was measured using a Malvern PANalytical X'pert PRO Material Powder Diffractometer (with 45 kW and 40 mA using Cu K$_\alpha$ radiation with λ = 1.5406 Å). The pattern was recorded in transmission mode from $2\theta = 2.5^\circ$ to 40° with a step scan of 0.03° counting for 200 s at each step. This diffractometer was equipped with a capillary spinner and the sample was placed inside a borosilicate glass capillary with an outer diameter of 0.7 mm. Elemental analyses (C, H, N) were carried out on a Thermo Scientific Flash 2000 CHNS Analyser. Melting points were measured on a Stuart Academic SMP10 melting point apparatus. FTIR-ATR spectra were recorded on a high-resolution spectrometer FT-IR PerkinElmer spectrum One equipped with a universal attenuated total reflectance (ATR) accessory with a diamond window in the range of 4000–500 cm^{-1}. ^{1}H NMR, ^{11}B NMR, ^{11}B{^{1}H} NMR and ^{13}C{^{1}H} NMR spectra were recorded on a NMR-FT Bruker 400 MHz spectrometer using deuterated acetonitrile (CD_3CN) at 25 °C. Chemical shifts are reported in ppm and referenced to the residual solvent peak for ^{1}H and ^{13}C{^{1}H} NMR or to $BF_3{\cdot}OEt_2$ as an external standard for ^{11}B and ^{11}B{^{1}H} NMR. Chemical shifts are reported in ppm and coupling constants in Hertz. Multiplets nomenclature is as follows: s, singlet; d, doublet; t, triplet; br, broad; m, multiplet.

The electronic spectra in CH_3CN (1.45×10^{-5}–6.5×10^{-5} M) were run on a JASCO V-780 UV-visible/NIR spectrophotometer with a quartz cell having a path length of 1 cm in the range of 190–600 nm. Solid-state electronic spectra were run on a JASCO V-780 UV-visible/NIR spectrophotometer equipped with a 60 mm integrating sphere model ISN-901i/A001461872. Solid-state emission and excitation spectra were run on a Nanolog™ Horib Jobin Yvon IHR320 fluorimeter. Quantum yields for compounds **1–4** in the solid state were measured on a Hammatsu Absolute PL Quantum Yield Spectometer C9920-O2G.

Crystallographic data

Crystallographic data of **L3** and compounds **1–4** is gathered in Table 1. Suitable crystals for X-ray elucidation were obtained *via* recrystallization of the products in THF (**L3**) or dry CH_3CN (**1–4**).

Crystals for X-ray Diffraction (XRD) were prepared under inert conditions immersed in perfluoropolyether or paratone as protecting oil for manipulation. Suitable crystals for **L3**, **1** and **3** were mounted on MiTeGen Micromounts™, and used for data collection at BL13 (XALOC)[124] at the ALBA synchrotron with an undulator source and channel-cut Si(111) monochromator and Kirkpatrick–Baez focusing mirrors with a selected wavelength of 0.72932 Å. An MD2M-Maatel diffractometer fitted with a Dectris Pilatus 6M detector was employed. The sample was kept at 100 K with an Oxford Cryosystems 700 series Cryostream. Crystallographic data for **2** and **4** were collected with a Bruker D8 Venture diffractometer with graphite monochromated MoKα radiation (λ = 0.71073 Å).

The structure for **L3** was solved with the ShelXT 2014/5 (Sheldrick, 2014) structure solution program using the direct phasing methods solution method and by using Olex2 as the graphical interface.[125] The model was refined with version 2016/6 of ShelXL using Least Squares minimisation.[126] The data for **1–4** were processed with APEX3 suite (Bruker APEX3. *APEX3 V2019.1*; Bruker-AXS: Madison, WI, USA, 2019). The structures were solved by Intrinsic Phasing using the ShelXT program,[126] which revealed the position of all non-hydrogen atoms. These atoms were refined on F^2 by a full-matrix least-squares procedure using anisotropic displacement parameter.[126] All hydrogen atoms were located in difference Fourier maps and included as fixed contributions riding on attached atoms with isotropic thermal displacement parameters 1.2 or 1.5 times those of the respective atom. The OLEX2 software was used as a graphical interface.[125] CCDC 204836 and 2050921–2050924.†

Computational details

To analyse the electronic structure and the nature of the excited states, time-dependent DFT calculations were performed by using the implementation of such approach in Gaussian16 program.[106] After some test, B3LYP functional[107,108] was selected because it provided a better agreement with the experimental data than other common exchange–correlation functional. An all electron Def2TZV basis set was employed in the calculations.[109] The calculations were performed for the discrete molecules **2** and **3**. To compare with the experimental absorption data, the calculations were carried out using both the experimental and also the optimized structures. The TDDFT calculations were employed only for the discrete molecules because for periodic structures would be mandatory to employ discrete models that usually lead to non-realistic results. The deexcitations energies are calculated by optimizing the structure of the excited triplet state and using such optimized geometry to perform a singlet calculation. Such procedure is employed because TDDFT calculations must be performed in the singlet ground state to extract the vertical excitation energies.

Conflicts of interest

There are no conflicts to declare.

Acknowledgements

This work was financially supported by MICINN (PID2019-106832RB-I00, PGC2018-093863-B-C21), MICINN through the

Severo Ochoa Program for Centers of Excellence for the FUNFUTURE (CEX2019-000917-S and MDM-2017-0767 projects) and the Generalitat de Catalunya (2017/SGR/1720 and SGR2017-1289). D. Ch.-L. acknowledges funding by project no. PGC2018-102047-B-I00 (MCIU/AEI/FEDER, UE). J. Soldevila-Sanmartín is enrolled in the UAB PhD program and acknowledges the PIF pre-doctoral Fellowship from the UAB for his pre-doctoral grant (no. 19032/2). E. R. acknowledges computer resources, technical expertise and assistance provided by the CSUC. We thank Prof. D. Ruiz and Dr C. Roscini for the quantum yield measurements. The present publication is dedicated to Prof. Elena Shubina on the occasion of her 70th birthday.

References

1 V. W.-W. Yam and K. K.-W. Lo, *Chem. Soc. Rev.*, 1999, **28**, 323–334.
2 A. Barbieri, G. Accorsi and N. Armaroli, *Chem. Commun.*, 2008, 2185.
3 E. Cariati, D. Roberto, R. Ugo, P. C. Ford, S. Galli and A. Sironi, *Chem. Mater.*, 2002, **14**, 5116–5123.
4 P. C. Ford, E. Cariati and J. Bourassa, *Chem. Rev.*, 1999, **99**, 3625–3648.
5 V. W.-W. Yam, V. K.-M. Au and S. Y.-L. Leung, *Chem. Rev.*, 2015, **115**, 7589–7728.
6 J. Troyano, F. Zamora and S. Delgado, *Chem. Soc. Rev.*, 2021, **50**, 4606–4628.
7 J. M. Busch, D. S. Koshelev, A. A. Vashchenko, O. Fuhr, M. Nieger, V. V. Utochnikova and S. Bräse, *Inorg. Chem.*, 2021, **60**, 2315–2332.
8 C. Gourlaouen, A. Hamano, K. Takano and C. Daniel, *ChemPhysChem*, 2021, **22**, 509–515.
9 R. Giereth, A. K. Mengele, W. Frey, M. Kloß, A. Steffen, M. Karnahl and S. Tschierlei, *Chem. – Eur. J.*, 2020, **26**, 2675–2684.
10 J. Li, L. Wang, Z. Zhao, X. Li, X. Yu, P. Huo, Q. Jin, Z. Liu, Z. Bian and C. Huang, *Angew. Chem., Int. Ed.*, 2020, **59**, 8210–8217.
11 C. Bizzarri, E. Spuling, D. M. Knoll, D. Volz and S. Bräse, *Coord. Chem. Rev.*, 2018, **373**, 49–82.
12 W. Liu, Y. Fang and J. Li, *Adv. Funct. Mater.*, 2018, **28**, 1705593.
13 D. Volz, Y. Chen, M. Wallesch, R. Liu, C. Fléchon, D. M. Zink, J. Friedrichs, H. Flügge, R. Steininger, J. Göttlicher, C. Heske, L. Weinhardt, S. Bräse, F. So and T. Baumann, *Adv. Mater.*, 2015, **27**, 2538–2543.
14 M. Alkan-Zambada, S. Keller, L. Martínez-Sarti, A. Prescimone, J. M. Junquera-Hernández, E. C. Constable, H. J. Bolink, M. Sessolo, E. Ortí and C. E. Housecroft, *J. Mater. Chem. C*, 2018, **6**, 8460–8471.
15 Y. Liu, S.-C. Yiu, C.-L. Ho and W.-Y. Wong, *Coord. Chem. Rev.*, 2018, **375**, 514–557.
16 J. Conesa-Egea, F. Zamora and P. Amo-Ochoa, *Coord. Chem. Rev.*, 2019, **381**, 65–78.
17 O. S. Wenger, *Chem. Rev.*, 2013, **113**, 3686–3733.
18 R. Peng, M. Li and D. Li, *Coord. Chem. Rev.*, 2010, **254**, 1–18.
19 Y.-D. Yu, L.-B. Meng, Q.-C. Chen, G.-H. Chen and X.-C. Huang, *New J. Chem.*, 2018, **42**, 8426–8437.
20 C. Slabbert and M. Rademeyer, *Coord. Chem. Rev.*, 2015, **288**, 18–49.
21 Q. Benito, X. F. Le Goff, G. Nocton, A. Fargues, A. Garcia, A. Berhault, S. Kahlal, J.-Y. Saillard, C. Martineau, J. Trébosc, T. Gacoin, J.-P. Boilot and S. Perruchas, *Inorg. Chem.*, 2015, **54**, 4483–4494.
22 H. D. Hardt and A. Pierre, *Z. Anorg. Allg. Chem.*, 1973, **402**, 107–112.
23 E. I. Musina, A. V. Shamsieva, I. D. Strelnik, T. P. Gerasimova, D. B. Krivolapov, I. E. Kolesnikov, E. V. Grachova, S. P. Tunik, C. Bannwarth, S. Grimme, S. A. Katsyuba, A. A. Karasik and O. G. Sinyashin, *Dalton Trans.*, 2016, **45**, 2250–2260.
24 D. M. Zink, T. Baumann, J. Friedrichs, M. Nieger and S. Bräse, *Inorg. Chem.*, 2013, **52**, 13509–13520.
25 L. Maini, P. P. Mazzeo, F. Farinella, V. Fattori and D. Braga, *Faraday Discuss.*, 2014, **170**, 93–107.
26 W.-F. Fu, X. Gan, C.-M. Che, Q.-Y. Cao, Z.-Y. Zhou and N. N.-Y. Zhu, *Chem. – Eur. J.*, 2004, **10**, 2228–2236.
27 D. M. Zink, T. Grab, T. Baumann, M. Nieger, E. C. Barnes, W. Klopper and S. Bräse, *Organometallics*, 2011, **30**, 3275–3283.
28 Z. Liu, P. I. Djurovich, M. T. Whited and M. E. Thompson, *Inorg. Chem.*, 2012, **51**, 230–236.
29 S. Naik, J. T. Mague and M. S. Balakrishna, *Inorg. Chem.*, 2014, **53**, 3864–3873.
30 K. Chen, J. Shearer and V. J. Catalano, *Inorg. Chem.*, 2015, **54**, 6245–6256.
31 E. W. Emerson, M. F. Cain, M. D. Sanderson, C. B. Knarr, D. S. Glueck, J. C. Ahern, H. E. Patterson and A. L. Rheingold, *Inorg. Chim. Acta*, 2015, **427**, 168–172.
32 E. Cariati, E. Lucenti, C. Botta, U. Giovanella, D. Marinotto and S. Righetto, *Coord. Chem. Rev.*, 2016, **306**, 566–614.
33 X. Zhang, W. Liu, G. Z. Wei, D. Banerjee, Z. Hu and J. Li, *J. Am. Chem. Soc.*, 2014, **136**, 14230–14236.
34 N. Mézailles, P. Le Floch, K. Waschbüsch, L. Ricard, F. Mathey and C. P. Kubiak, *J. Organomet. Chem.*, 1997, **541**, 277–283.
35 S. Daly, M. F. Haddow, A. G. Orpen, G. T. A. Rolls, D. F. Wass and R. L. Wingad, *Organometallics*, 2008, **27**, 3196–3202.
36 R. Ahuja, M. Nethaji and A. G. Samuelson, *Inorg. Chim. Acta*, 2011, **372**, 220–226.
37 M. Scherer, D. Stein, F. Breher, J. Geier, H. Schönberg and H. Grützmacher, *Z. Anorg. Allg. Chem.*, 2005, **631**, 2770–2774.
38 E. Kühnel, I. V. Shishkov, F. Rominger, T. Oeser and P. Hofmann, *Organometallics*, 2012, **31**, 8000–8011.
39 X. Han, Z. Weng, D. J. Young, G.-X. Jin and T. S. Andy Hor, *Dalton Trans.*, 2014, **43**, 1305–1312.

40 K. A. Vinogradova, V. P. Krivopalov, E. B. Nikolaenkova, N. V. Pervukhina, D. Y. Naumov, M. I. Rakhmanova, E. G. Boguslavsky, L. A. Sheludyakova and M. B. Bushuev, *Polyhedron*, 2013, **57**, 1–13.
41 J. C. Li, H. X. Li, H. Y. Li, W. J. Gong and J. P. Lang, *Cryst. Growth Des.*, 2016, **16**, 1617–1625.
42 M. Yang, X.-L. Chen and C.-Z. Lu, *Dalton Trans.*, 2019, **48**, 10790–10794.
43 S.-Z. Zhan, T. Feng, W. Lu, M. R. Razali and D. Li, *Cryst. Growth Des.*, 2018, **18**, 7663–7673.
44 J.-H. Wang, M. Li, J. Zheng, X.-C. Huang and D. Li, *Chem. Commun.*, 2014, **50**, 9115–9118.
45 F. Wu, H. Tong, K. Wang, X. Zhang, J. Zhang, W.-K. Wong and X. Zhu, *J. Coord. Chem.*, 2016, **69**, 926–933.
46 A. Tarassoli, V. Nobakht, E. Baladi, L. Carlucci and D. M. Proserpio, *CrystEngComm*, 2017, **19**, 6116–6126.
47 J. He, J. Duan, H. Shi, J. Huang, J. Huang, L. Yu, M. Zeller, A. D. Hunter and Z. Xu, *Inorg. Chem.*, 2014, **53**, 6837–6843.
48 W.-X. Wang, L. Wang, H.-X. Li, H.-Y. Li and J.-P. Lang, *Z. Anorg. Allg. Chem.*, 2013, **639**, 618–625.
49 H.-Y. Li, Y. Zhang, Y.-C. Ding, M. Wang, L.-X. Dai and J.-P. Lang, *J. Mol. Struct.*, 2011, **996**, 90–94.
50 J. Soldevila-Sanmartín, X. Montaner, T. Calvet, M. Font-Bardia and J. Pons, *Polyhedron*, 2020, 114686.
51 M. Guerrero, S. Vázquez, J. A. Ayllón, T. Calvet, M. Font-Bardia and J. Pons, *ChemistrySelect*, 2017, **2**, 632–639.
52 A. M. López Marzo, M. Guerrero, T. Calvet, M. Font-Bardia, E. Pellicer, M. D. Baró, J. Pons and J. Sort, *RSC Adv.*, 2015, **5**, 32369–32375.
53 M. Guerrero, J. Pons, J. Ros, M. Font-Bardia, O. Vallcorba, J. Rius, V. Branchadell and A. Merkoçi, *CrystEngComm*, 2011, **13**, 6457.
54 M. Guerrero, J. Pons and J. Ros, *J. Organomet. Chem.*, 2010, **695**, 1957–1960.
55 M. Guerrero, J. Pons, M. Font-Bardia, T. Calvet and J. Ros, *Aust. J. Chem.*, 2010, **63**, 958.
56 M. Y. Tsang, C. Viñas, F. Teixidor, J. G. Planas, N. Conde, R. SanMartin, M. T. Herrero, E. Dominguez, A. Lledos, P. Vidossich and D. Choquesillo-Lazarte, *Inorg. Chem.*, 2014, **53**, 9284–9295.
57 J. Planas, F. Teixidor and C. Viñas, *Crystals*, 2016, **6**, 50.
58 F. Di Salvo, M. Y. Tsang, F. Teixidor, C. Viñas, J. G. Planas, J. Crassous, N. Vanthuyne, N. Aliaga-Alcalde, E. Ruiz, G. Coquerel, S. Clevers, V. Dupray, D. Choquesillo-Lazarte, M. E. Light and M. B. Hursthouse, *Chem. – Eur. J.*, 2014, **20**, 1081–1090.
59 F. Di Salvo, F. Teixidor, C. Viñas and J. Giner Planas, *Z. Anorg. Allg. Chem.*, 2013, **639**, 1194–1198.
60 F. Di Salvo, F. Teixidor, C. Viñas, J. Giner Planas, M. E. Light, M. B. Hursthouse and N. Aliaga-Alcalde, *Cryst. Growth Des.*, 2012, **12**, 5720–5736.
61 G. Grach, G. Pieters, A. Dinut, V. Terrasson, R. Medimagh, A. Bridoux, V. Razafimahaleo, A. Gaucher, S. Marque, J. Marrot, D. Prim, R. Gil, J. Giner Planas, C. Vinas, I. Thomas, J.-P. Roblin and Y. Troin, *Organometallics*, 2011, **30**, 4074–4086.
62 F. Di Salvo, J. G. Planas, C. Vinas, F. Teixidor, M. E. Light and M. B. Hursthouse, *Acta Crystallogr., Sect. A: Found. Adv.*, 2011, **67**, C368.
63 V. Terrasson, J. G. Planas, C. Viñas, F. Teixidor, D. Prim, M. E. Light and M. B. Hursthous, *Organometallics*, 2010, **29**, 4130–4134.
64 J. Plesek, *Chem. Rev.*, 1992, **92**, 269–278.
65 F. Teixidor, C. Viñas, A. Demonceau and R. Nuñez, *Pure Appl. Chem.*, 2003, **75**, 1305–1313.
66 R. N. Grimes, *Carboranes*, 2nd edn, 2011.
67 F. Teixidor, G. Barberà, A. Vaca, R. Kivekäs, R. Sillanpää, J. Oliva and C. Viñas, *J. Am. Chem. Soc.*, 2005, **127**, 10158–10159.
68 J. Poater, M. Solà, C. Viñas and F. Teixidor, *Angew. Chem., Int. Ed.*, 2014, **53**, 12191–12195.
69 J. Poater, C. Viñas, I. Bennour, S. Escayola, M. Solà and F. Teixidor, *J. Am. Chem. Soc.*, 2020, **142**, 9396–9407.
70 M. Scholz and E. Hey-Hawkins, *Chem. Rev.*, 2011, **111**, 7035–7062.
71 L. Schwartz, L. Eriksson, R. Lomoth, F. Teixidor, C. Viñas and S. Ott, *Dalton Trans.*, 2008, 2379–2381.
72 R. Núñez, P. Farràs, F. Teixidor, C. Viñas, R. Sillanpää and R. Kivekäs, *Angew. Chem., Int. Ed.*, 2006, **45**, 1270–1272.
73 F. Teixidor, R. Núñez, C. Viñas, R. Sillanpää and R. Kivekäs, *Angew. Chem., Int. Ed.*, 2000, **39**, 4290–4292.
74 A. M. Spokoyny, C. W. Machan, D. J. Clingerman, M. S. Rosen, M. J. Wiester, R. D. Kennedy, C. L. Stern, A. A. Sarjeant and C. A. Mirkin, *Nat. Chem.*, 2011, **3**, 590–596.
75 L. E. Riley, T. Krämer, C. L. McMullin, D. Ellis, G. M. Rosair, I. B. Sivaev and A. J. Welch, *Dalton Trans.*, 2017, **46**, 5218–5228.
76 F. Tan, A. López-Periago, M. E. Light, J. Cirera, E. Ruiz, A. Borrás, F. Teixidor, C. Viñas, C. Domingo and J. G. Planas, *Adv. Mater.*, 2018, **30**, 1800726.
77 M. A. Fox and A. K. Hughes, *Coord. Chem. Rev.*, 2004, **248**, 457–476.
78 J. G. Planas, C. Vinas, F. Teixidor, A. Comas-Vives, G. Ujaque, A. Lledos, M. E. Light and M. B. Hursthouse, *J. Am. Chem. Soc.*, 2005, **127**, 15976–15982.
79 R. Nunez, M. Tarres, A. Ferrer-Ugalde, F. F. de Biani and F. Teixidor, *Chem. Rev.*, 2016, **116**, 14307–14378.
80 S. Mukherjee and P. Thilagar, *Chem. Commun.*, 2016, **52**, 1070–1093.
81 F. Teixidor and C. Viñas, in *Science of Synthesis*, ed. D. E. Kaufmann and D. S. Matteson, Thieme, Stuttgart, 2005, vol. 6, pp. 1275–1325.
82 J. Ochi, K. Tanaka and Y. Chujo, *Angew. Chem., Int. Ed.*, 2020, **59**, 9841–9855.
83 H. Naito, K. Nishino, Y. Morisaki, K. Tanaka and Y. Chujo, *Angew. Chem., Int. Ed.*, 2017, **56**, 254–259.
84 D. Tu, S. Cai, C. Fernandez, H. Ma, X. Wang, H. Wang, C. Ma, H. Yan, C. Lu and Z. An, *Angew. Chem., Int. Ed.*, 2019, **58**, 9129–9133.
85 X. Wei, M.-J. Zhu, Z. Cheng, M. Lee, H. Yan, C. Lu and J.-J. Xu, *Angew. Chem., Int. Ed.*, 2019, **58**, 3162–3166.

86 J. Cabrera-Gonzalez, C. Vinas, M. Haukka, S. Bhattacharyya, J. Gierschner and R. Nunez, *Chem. – Eur. J.*, 2016, **22**, 13588–13598.
87 J. Cabrera-Gonzalez, S. Bhattacharyya, B. Milian-Medina, F. Teixidor, N. Farfan, R. Arcos-Ramos, V. Vargas-Reyes, J. Gierschner and R. Nunez, *Eur. J. Inorg. Chem.*, 2017, 4575–4580.
88 J. Cabrera-González, M. Chaari, F. Teixidor, C. Viñas and R. Núñez, *Molecules*, 2020, **25**, 1210.
89 M. Chaari, Z. Kelemen, D. Choquesillo-Lazarte, F. Teixidor, C. Viñas and R. Núñez, *Inorg. Chem. Front.*, 2020, **7**, 2370–2380.
90 M. Chaari, Z. Kelemen, D. Choquesillo-Lazarte, N. Gaztelumendi, F. Teixidor, C. Viñas, C. Nogués and R. Núñez, *Biomater. Sci.*, 2019, **7**, 5324–5337.
91 M. Chaari, Z. Kelemen, J. G. Planas, F. Teixidor, D. Choquesillo-Lazarte, A. Ben Salah, C. Viñas and R. Núñez, *J. Mater. Chem. C*, 2018, **6**, 11336–11347.
92 M. T. Güllüoglu, M. Ozduran, M. Kurt, S. Kalaichelvan and N. Sundaraganesan, *Spectrochim. Acta, Part A*, 2010, **76**, 107–114.
93 G. Zerbi and C. Alberti, *Spectrochim. Acta*, 1962, **18**, 407–423.
94 S. Demir, B. Eren and M. Hołyńska, *J. Mol. Struct.*, 2015, **1081**, 304–310.
95 C. R. Groom, I. J. Bruno, M. P. Lightfoot and S. C. Ward, *Acta Crystallogr., Sect. B: Struct. Sci., Cryst. Eng. Mater.*, 2016, **72**, 171–179.
96 A. Neshat, R. B. Aghakhanpour, P. Mastrorilli, S. Todisco, F. Molani and A. Wojtczak, *Polyhedron*, 2018, **154**, 217–228.
97 E. I. Musina, A. V. Shamsieva, I. D. Strelnik, T. P. Gerasimova, D. B. Krivolapov, I. E. Kolesnikov, E. V. Grachova, S. P. Tunik, C. Bannwarth, S. Grimme, S. A. Katsyuba, A. A. Karasik and O. G. Sinyashin, *Dalton Trans.*, 2016, **45**, 2250–2260.
98 T. N. Sorrell and A. S. Borovik, *Inorg. Chem.*, 1987, **26**, 1957–1964.
99 M. Vitale and P. C. Ford, *Coord. Chem. Rev.*, 2001, **219**, 3–16.
100 A. Acosta, J. I. Zink and J. Cheon, *Inorg. Chem.*, 2000, **39**, 427–432.
101 V. Balzani, G. Bergamini, S. Campagna and F. Puntoriero, in *Photochemistry and Photophysics of Coordination Compounds I*, ed. V. Balzani and S. Campagna, Springer Berlin Heidelberg, Berlin, Heidelberg, 2007, pp. 1–36.
102 J. Zhao, D. Shi, H. Cheng, L. Chen, P. Ma and J. Niu, *Inorg. Chem. Commun.*, 2010, **13**, 822–827.
103 A. V. Artem'ev, D. G. Samsonenko and O. V. Antonova, *Polyhedron*, 2018, **151**, 171–176.
104 A. Aguirrechu-Comerón, R. Hernández-Molina, P. Rodríguez-Hernández, A. Muñoz, U. R. Rodríguez-Mendoza, V. Lavín, R. J. Angel and J. Gonzalez-Platas, *Inorg. Chem.*, 2016, **55**, 7476–7484.
105 I. L. Malaestean, V. C. Kravtsov, J. Lipkowski, E. Cariati, S. Righetto, D. Marinotto, A. Forni and M. S. Fonari, *Inorg. Chem.*, 2017, **56**, 5141–5151.
106 J. López, J. G. Platas, U. R. Rodríguez-Mendoza, J. I. Martínez, S. Delgado, G. Lifante-Pedrola, E. Cantelar, R. Guerrero-Lemus, C. Hernández-Rodríguez and P. Amo-Ochoa, *Inorg. Chem.*, 2021, **60**, 1208–1219.
107 K. Hassanein, P. Amo-Ochoa, C. J. Gómez-García, S. Delgado, O. Castillo, P. Ocón, J. I. Martínez, J. Perles and F. Zamora, *Inorg. Chem.*, 2015, **54**, 10738–10747.
108 N. M. Khatri, M. H. Pablico-Lansigan, W. L. Boncher, J. E. Mertzman, A. C. Labatete, L. M. Grande, D. Wunder, M. J. Prushan, W. Zhang, P. S. Halasyamani, J. H. S. K. Monteiro, A. De Bettencourt-Dias and S. L. Stoll, *Inorg. Chem.*, 2016, **55**, 11408–11417.
109 D. Volz, D. M. Zink, T. Bocksrocker, J. Friedrichs, M. Nieger, T. Baumann, U. Lemmer and S. Bräse, *Chem. Mater.*, 2013, **25**, 3414–3426.
110 F. H. Allen, *Acta Crystallogr., Sect. B: Struct. Sci.*, 2002, **58**, 380–388.
111 K. Tsuge, Y. Chishina, H. Hashiguchi, Y. Sasaki, M. Kato, S. Ishizaka and N. Kitamura, *Coord. Chem. Rev.*, 2016, **306**, 636–651.
112 D. Volz, M. Wallesch, S. L. Grage, J. Göttlicher, R. Steininger, D. Batchelor, T. Vitova, A. S. Ulrich, C. Heske, L. Weinhardt, T. Baumann and S. Bräse, *Inorg. Chem.*, 2014, **53**, 7837–7847.
113 A. V. Artem'ev, D. G. Samsonenko and O. V. Antonova, *Polyhedron*, 2018, **151**, 171–176.
114 S. Demir, B. Eren and M. Hołyńska, *J. Mol. Struct.*, 2015, **1081**, 304–310.
115 S. Jana and S. Chattopadhyay, *Polyhedron*, 2014, **81**, 298–307.
116 Y.-D. Yu, L.-B. Meng, Q.-C. Chen, G.-H. Chen and X.-C. Huang, *New J. Chem.*, 2018, **42**, 8426–8437.
117 P. Boden, P. Di Martino-Fumo, J. Busch, F. Reahak, S. Steiger, O. Fuhr, M. Nieger, D. Volz, W. Klopper, S. Bräse and M. Gerhards, *Chem. – Eur. J.*, 2021, **27**, 5439–5452.
118 M. J. Frisch, G. W. Trucks, H. B. Schlegel, G. E. Scuseria, M. A. Robb, J. R. Cheeseman, G. Scalmani, V. Barone, G. A. Petersson, H. Nakatsuji, X. Li, M. Caricato, A. V. Marenich, J. Bloino, B. G. Janesko, R. Gomperts, B. Mennucci, H. P. Hratchian, J. V. Ortiz, A. F. Izmaylov, J. L. Sonnenberg, D. Williams, F. Ding, F. Lipparini, F. Egidi, J. Goings, B. Peng, A. Petrone, T. Henderson, D. Ranasinghe, V. G. Zakrzewski, J. Gao, N. Rega, G. Zheng, W. Liang, M. Hada, M. Ehara, K. Toyota, R. Fukuda, J. Hasegawa, M. Ishida, T. Nakajima, Y. Honda, O. Kitao, H. Nakai, T. Vreven, K. Throssell, J. A. Montgomery Jr, J. E. Peralta, F. Ogliaro, M. J. Bearpark, J. J. Heyd, E. N. Brothers, K. N. Kudin, V. N. Staroverov, T. A. Keith, R. Kobayashi, J. Normand, K. Raghavachari, A. P. Rendell, J. C. Burant, S. S. Iyengar, J. Tomasi, M. Cossi, J. M. Millam, M. Klene, C. Adamo, R. Cammi, J. W. Ochterski, R. L. Martin, K. Morokuma, O. Farkas, J. B. Foresman and D. J. Fox, *Gaussian 16, Revision C.01*, Gaussian, Inc., Wallingford CT, 2016.
119 A. D. Becke, *J. Chem. Phys.*, 1993, **98**, 5648–5652.

120 F. Weigend and R. Ahlrichs, *Phys. Chem. Chem. Phys.*, 2005, **7**, 3297–3305.
121 F. Weigend, *Phys. Chem. Chem. Phys.*, 2006, **8**, 1057–1065.
122 S.-Z. Zhan, X. Jiang, J. Zheng, X.-D. Huang, G.-H. Chen and D. Li, *Dalton Trans.*, 2018, **47**, 3679–3683.
123 W. G. Haanstra, W. L. Driessen, J. Reedijk, U. Turpeinen and R. Hämäläinenn, *J. Chem. Soc., Dalton Trans.*, 1989, 2309–2314.
124 J. Juanhuix, F. Gil-Ortiz, G. Cuni, C. Colldelram, J. Nicolas, J. Lidon, E. Boter, C. Ruget, S. Ferrer and J. Benach, *J. Synchrotron Radiat.*, 2014, **21**, 679–689.
125 O. V. Dolomanov, L. J. Bourhis, R. J. Gildea, J. A. K. Howard and H. Puschmann, *J. Appl. Crystallogr.*, 2009, **42**, 339–341.
126 G. Sheldrick, *Acta Crystallogr., Sect. C: Struct. Chem.*, 2015, **71**, 3–8.